Biointerface Research in Applied Chemistry
Open-Access Journal (ISSN: 2069-5837)

*Article*
**Volume 13, Issue 5, 2023, 498**
https://doi.org/10.33263/BRIAC135.498

# Structural, Infrared and Raman Spectroscopy Reinvestigation, and Theoretical Optoelectronic Properties of Hydrazinium (1+) Hexafluorosilicate $(N_2H_5)_2SiF_6$

**Ali Ouasri [1,2,*], Imane Hamideddine [3], Houda Jebari [3], Ali Rhandour [2], Najim Tahiri [3], Omar El Bounagui [3], Hamid Ez-Zahraouy [3]**

[1] Laboratoire (ReSIP), Centre Régional des Métiers de l'Education et de la Formation, Madinat Al Irfane, Souissi, B.P. 6210 Rabat, Morocco
[2] Equipe de Physico-Chimie des Matériaux Inorganiques, Université Ibn Tofail, Faculté des Sciences, B.P. 133, 14000 Kenitra, Morocco
[3] Laboratory of Condensed Matter and Interdisciplinary Sciences, Unite de Recherche Labelliseìe CNRST, URL-CNRST-17, Faculty of Sciences, Mohammed V University of Rabat, Morocco
* Correspondence: aouasri@yahoo.fr (A.O.);

Scopus Author ID 56001570100
**Received: 12.09.2022; Accepted: 30.10.2022; Published: 6.01.2023**

**Abstract:** The material $(N_2H_5)_2SiF_6$ was reinvestigated by XRD, IR, and Raman spectroscopy. It crystallizes in the monoclinic space group $P2_1/n$ (Z=2). The characteristic bands in FT-IR (450-4000) $cm^{-1}$ and FT-Raman (50-3500) $cm^{-1}$ spectra were interpreted using factor group analysis considering the $D_2$ factor group, in which $SiF_6^{2-}$ anions and $N_2H_5^+$ cations occupied $C_i$ and $C_1$ symmetry sites, respectively. Against the previous assignment, the Infrared bands (651, 474, 435 $cm^{-1}$) are not due to the Raman active modes [$\nu_1$ (Si-F), $\nu_2$ (Si-F), and $\nu_5$ (F-Si-F)] of $SiF_6^{2-}$ anion, theoretically not infrared active in the $P2_1/n$ space group. The electronic structure, optical, photocatalytic, and thermoelectric properties of $(N_2H_5)_2SiF_6$ are investigated using the Full-Potential Linearized Augmented Plane Wave (FP-LAPW) method based on the density functional theory (DFT) as implemented in Wien2k package. Hence, the direct band gap energy, with valence band (VB) maximum and conduction band (CB) minimum too located at point Γ, is calculated at 7.04 eV. The photocatalytic reaction mechanism of $(N_2H_5)_2SiF_6$ is described. The optical properties comprising absorption, conductivity, reflectivity, and refractivity index (1.2 for $\lambda > 200$ nm), were evaluated versus wavelength (100-1000 nm). The high absorption coefficient ($50\times10^4$ $cm^{-1}$ in small wavelength) indicates absorption in the ultraviolet range. The optical conductivity, decreasing to zero for $\lambda > 200$ nm, implies a very high conductivity of this salt for high wavelength applications. The transport properties studied at ambient temperature show high electrical conductivity (2.04 $10^{18}$ $S.cm^{-1}.s^{-1}$), high thermal conductivity (2.81 $10^{13}$ $W.m^{-1}.K^{-1}.s^{-1}$), and low and positive Seebeck coefficient (1.67 $10^{-4}$ $V.K^{-1}$) of the perspective material $(N_2H_5)_2SiF_6$.

**Keywords:** IR; Raman; FP-LAPW method; optoelectronic; photocatalytic; thermoelectric properties.



## 1. Introduction

Hybrid materials have attracted more attention to research merging characteristics of both organic and inorganic components [1-9]. Especially, 2D perovskites were investigated for

their exceptional properties, such as high optical absorption coefficients, structural diversity, and tuneable bandgaps, which allow their application as active light-absorbing materials to develop solar cells and photodetectors [6-9].

Hydrazinium hexafluorometalate salts, belonging to this large family of hybrid materials, were found to adopt two different formulas, $N_2H_6MCl_6$ [10–15] and $(N_2H_5)_2MF_6$ [16–21] (M: Ga, Si, Ti, Zr, HF). The hydrazinium (2+) hexafluorosilicate $N_2H_6SiF_6$ structure at room temperature, orthorhombic of space group [Pbca, Z=4, a=7.605(1) Å, b=7.586(2) Å, c=8.543(1) Å], consisted of centrosymmetric $N_2H_6^{2+}$ and $SiF_6^{2-}$ ions arranged in a NaC1-type packing and linked by hydrogen bonds to two-dimensional $N_2H_6$…$SiF_6$ layers parallel to (001) [16]. X-ray, thermal, and vibrational studies were performed on other hydrazinium (1+) hexahalogenometallate salts, $(N_2H_5)_2ZrF_6$ and $(N_2H_5)_2HfF_6$ [17]. In $(N_2H_5)_2GeF_6$ [Monoclinic, $P2_1/n$, Z=2, a=6.015(2) Å, b=5.249(1) Å, c=11.181(2) Å β=100.15 (2)°] [18], $N_2H_5^+$ cations and $GeF_6^{2-}$ anions are linked via hydrogen bonds N-H***F and N-H***N.

The hydrazinium (1+) hexafluorosilicate $(N_2H_5)_2SiF_6$ crystal was studied by spectroscopy and X-ray powder analyses based on its isostructural monoclinic $(N_2H_5)_2GeF_6$ [a = 5.96(2) Å, b = 5.19(l) Å, c = 10.99(5) Å, β=100.1(3)°] [20]; it was synthesized by mixing an aqueous solution of $N_2H_6SiF_6$, and diluted hydrazinium hydrate (pH = 5), which is different from the method we used to synthesis this crystal [21]. Gantar [20] assigned the Infrared bands observed at 638, 464, and 419 $cm^{-1}$ to the anionic $SiF_6^{2-}$ Raman active modes: $\nu_1$ (Si-F), $\nu_2$ (Si-F) and $\nu_5$ (F-Si-F), which are theoretically not infrared active in the $P2_1/n$ space group.

Recently, the $(N_2H_5)_2SiF_6$ crystal was synthesized by another method, and its structure was fully determined in the monoclinic space group $P2_1/n$ (Z=2) [a=5.9496(3) Å, b=5.2484(2) Å, c=11.0029(5) Å, β=100.245(1)°, V=338.10(3) $Å^3$] [21]. The $N_2H_5^+$ cation and the slightly distorted $SiF_6^{2-}$ octahedron anion is linked together via hydrogen bonds N-H***F ranging from 2.02 to 2.52 Å (for H***F). The $SiF_6^{2-}$ octahedra are arranged in wire parallel to [1 0 0] direction with Si–F distances [1.6777 (4) –1.7100 (4) Å], while the cations, linked together by hydrogen bonds N–H***N, form zigzag chains were running along [0 1 0] direction [21]. Hirshfeld surface and fingerprints plots analyses showed that the F···H (75.5%), H···H (13.6%), N···H (8.4 %), F···F (1.9%), and F···N (0.6%) contacts involved in $(N_2H_5)_2SiF_6$ crystal packing [21], which implied that F···H contacts are prominent in the crystal packing, accordingly to strong hydrogen bonding resulted in X-ray analysis. The $(N_2H_5)_2SiF_6$ compound was found to be efficient in the catalysis field [22, 23].

In the present work, we report on the synthesis of hydrazinium (1+) hexafluorosilicate $(N_2H_5)_2SiF_6$ crystals, its fully determined structure using X-ray diffraction at room temperature, and the Infrared-Raman spectra to carry out a rigorous assignment, particularly the Infrared bands of anionic parts by the theoretical group analyses. On the other hand, we investigate the optoelectronic, photocatalytic, and thermoelectric properties of $(N_2H_5)_2SiF_6$ compound. Calculations of these properties were achieved by adopting the full-potential linearized augmented plane wave (FP-LAPW) [24] method in the density functional theory framework with the generalized gradient approximation (GGA).

## 2. Materials and Methods

### *2.1. Experimental methods.*

Hydrazinium (1+) hexafluorosilicate $(N_2H_5)_2SiF_6$ crystal was recently obtained by slow evaporation, at room temperature, of aqueous solution containing stoichiometric (2:1) amounts of hydrazine $NH_2NH_2$ and $H_2SiF_6$ acid [21]. The recent synthesis method, different from that published elsewhere [20], consists of mixing the $H_2SiF_6$ acid (34 % in weight) with the pure $NH_2NH_2$ (100 %) in minimal distilled water volume. The evaporation of the obtained solution at ambient temperature for a few weeks gives single colorless crystals of $(N_2H_5)_2SiF_6$. The reaction equations adopted for this synthesis are described as the following:

$$NH_2NH_{2\,(aq)} + H_2O \rightarrow [OH^-_{(aq)} +, {}^+NH_3NH_{2\,(aq)}]$$

$$2\,[OH^-_{(aq)}\,, {}^+NH_3NH_{2\,(aq)}] + H_2SiF_6 \longrightarrow (N_2H_5)_2SiF_6 + 2H_2O$$

The Infrared spectrum was recorded in the (450–4000 $cm^{-1}$) spectral range with a 4 $cm^{-1}$ resolution (20 scans) by using a VERTEX 70 FTIR spectrometer (produced by BRUKER Optics). The MIR Transmission Technique was used to record the IR spectrum. The Raman spectrum (50–3500 $cm^{-1}$) was recorded at room temperature by the FT-Raman Technique using a RAM spectrometer coupled with the VERTEX 70, equipped with an Nd Yag (633 nm) as the exciting source Laser (puissance laser: 8 mW). The spectral resolution was 4 $cm^{-1}$ (64 scans), and the band positions were accurate to ± 1 $cm^{-1}$.

### *2.2. Computational methods.*

The theoretical study of the synthesized compound is investigated using the Full-Potential Linearized Augmented Plane Wave method (FP-LAPW) [24] as implemented in Wien2k package [25] based on the density functional theory (DFT). The optoelectronic properties, including electronic and optical bandgap energies, the absorption coefficient, and the reflectivity of our compound were treated at T = 0 K, using the Generalized Gradient Approximation (GGA) [26]. The convergence criterion was fixed at $10^{-4}$ Ry and the convergence force to 1 mRy/a.u and 4×4×2 k-point in the irreducible wedge of the Brillion zone for optimization. The thermoelectric properties, including electrical conductivity, thermal conductivity, Seebeck coefficient, carrier mobility, and carrier's concentration of the studied compound, have been investigated at room temperature via the BoltzTraP package integrated into the WIEN2k package [25, 27].

## 3. Results and Discussion

### *3.1. Structural characteristics of $(N_2H_5)_2SiF_6$.*

In the crystal structure of $(N_2H_5)_2SiF_6$, illustrated in Figure 1, the distorted $SiF_6^{2-}$ isolated octahedra were propagating along the- axis direction, while the zigzag cationic chains were running along [0 1 0] direction [21]. In $SiF_6^{2-}$, there are F-Si-F *cis* angles varying in [89.26(2)-89.90(2)°], *trans* angle [179.999(17)°, 180°], and slightly deviated angles [90.10(2)°-90.74(2)°]; the three Si–F bond lengths are [1.6777 (4), 1.6785(4), 1.7101(4) Å]. The distortion parameters may be calculated as [28, 29]:

$$ID(Si-F)=\frac{\sum|SiF_i-SiF_m|}{6SiF_m}\cong 0.00843,\ \text{and}\ \Delta_{oct\times 10}{}^3=\frac{1}{6}\sum(\frac{SiF_i-SiF_m}{SiF_m})^2\cong 0.31935,$$

where Si-$F_m$ is the average bond length <Si-F>. The obtained values are considered the lowest values of bond-length distortion in the SiF62- octahedron, indicating that the anion is slightly distorted in this compound. These values are compared to that calculated for $[(CH_3)_4N]_2SiF_6$ at ID(*Si*–F) ≅ 0.0145 and $\Delta_{oct} \times 10^3$ = 0.37 [29], which indicates that $SiF_6^{2-}$ anions are more distorted in the $[(CH_3)_4N]_2SiF_6$ rather than in the $(N_2H_5)_2SiF_6$ structure. In table 1 are given characteristic cationic torsional angles (°) H-N-N-H in $(N_2H_5)_2SiF_6$. The torsional angles H1B-N1-N2-H2B (177.05°) and H1A-N1-N2-H2A [-174.09°] indicate that the $NH_2NH_3^+$ cation has deviated from its full trans conformation.

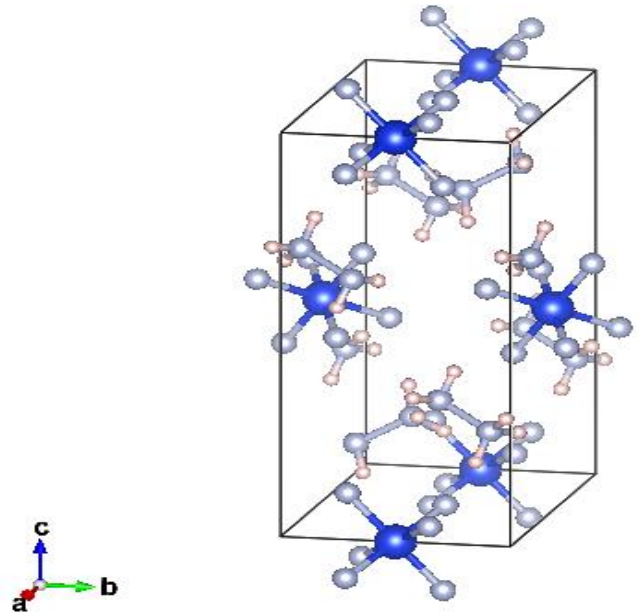


**Figure 1.** A tri-dimensional view of $(N_2H_5)_2SiF_6$ structure showing isolated inorganic octahedra and organic cations.

**Table 1.** Characteristic of cationic torsional angles (°) in $(N_2H_5)_2SiF_6$.

| Atom 1 | Atom 2 | Atom 3 | Atom 4 | Tors. angles (°) |
|---|---|---|---|---|
| H1A | N1 | N2 | H2A | -174.09 |
| H1A | N1 | N2 | H2B | -62.94 |
| H1B | N1 | N2 | H2A | 65.90 |
| H1B | N1 | N2 | H2B | 177.05 |
| H1C | N1 | N2 | H2A | -54.10 |
| H1C | N1 | N2 | H2B | 57.05 |

*3.2. X-ray diffraction patterns.*

The XRD pattern of the synthesized hydrazinium (1+) hexafluorosilicate $(N_2H_5)_2SiF_6$ is shown in Figure 2. The diffractogram notice that the sample crystallizes in the monoclinic structure with space group $P2_1/n$ (Z = 2). The refined cell parameters and cell volume mentioned in our previous work were found to be a = 5.9496(3) Å, b = 5.2484(2) Å, c =11.0029(5) Å, β = 100.245(1)°, V = 338.10 (3) $Å^3$ [21].

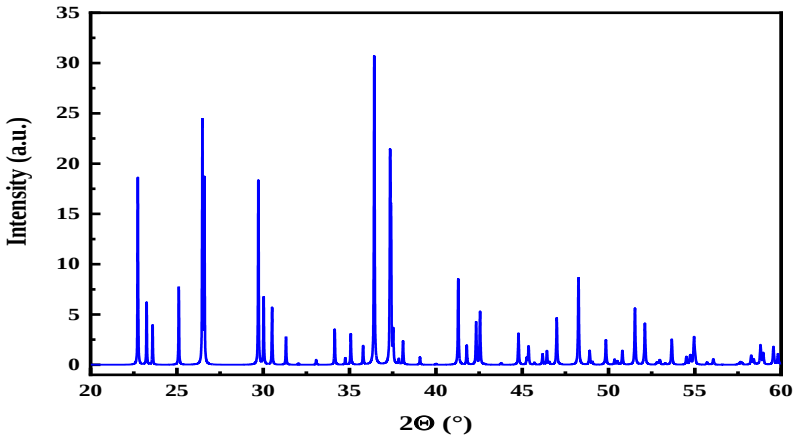


**Figure 2.** XRD pattern of the prepared $(N_2H_5)_2SiF_6$ compound.

*3.3.* Raman and Infrared spectra analysis.

3.3.1. Vibrational modes of $N_2H_5^+$ cation.

The free hydrazinium (+1) $NH_2$-$NH_3^+$ cation of $C_1$ symmetry displays 15 A' (Ra, IR) internal vibration modes, all Infrared and Raman active. In the crystal of space group $P2_1/n$ (Z = 2), factor group ($C_{2h}$), $NH_2$-$NH_3^+$ cations occupy the Wyckoff general positions 4e [21] corresponding to $C_1$ sites symmetry. So, there is any site group effect on the cationic vibration modes in the crystal. Each of 15 A' modes in the site group splits into 2 components by the crystal field effect (Davydov splitting effect) due to the existence of 2 cations per primitive unit cell (Table 2). The 60 internal modes of the cations in the crystal are described as 15 [$A_g$ (Ra) + $B_g$ (Ra) + $A_u$ (IR) + $B_u$ (IR)], all infrared and Raman actives with respect to the selection rules implying that ($A_g$ and $B_g$) modes are Raman active, and ($A_u$ and $B_u$) are infrared active.

**Table 2.** Correlation diagram of the $NH_2$-$NH_3^+$ cation internal vibrational modes in the crystal.

| Point group ($C_1$) | Site group ($C_1$) | Factor group ($C_{2h}$) |
|---|---|---|
| 15 A (Ra, IR) | 15 A (Ra, IR) | 15 $A_g$ (Ra) |
| | | 15 $A_u$ (IR) |
| | | 15 $B_g$ (Ra) |
| | | 15 $B_u$ (IR) |

3.3.2. Vibrational modes of $SiF_6^{2-}$ anions.

The free $SiF_6^{2-}$ anions ($O_h$ symmetry) possess 15 internal vibration modes described as: $1A_{1g}$ (Ra) +$1E_g$ (Ra) + $1F_{2g}$ (Ra) + $2F_{1u}$ (IR) + $1F_{2u}$ (IR) [15, 30-32]. The Raman-active ($A_{1g}$, $E_g$, $F_{2g}$) modes and those of $F_{1u}$ type-infrared active appear as single bands for an ideal octahedral anion, whereas the $F_{2u}$ modes are inactive. In the centrosymmetric crystal $(N_2H_5)_2SiF_6$ of $P2_1/n$ (Z = 2) space group, the $SiF_6^{2-}$ anions occupied the $C_i$ (2) sites symmetry [21]. Under the site effect (Table 3), the $A_{1g}$ [$\nu_1$ (Si-F)], $E_g$ [$\nu_2$ (Si-F)], and $F_{2g}$ [$\nu_5$ (F-Si-F)] modes are expected to be only Raman active with $A_g$ symmetry; the $E_g$ and $F_{2g}$ modes should split into two and three Raman active components, respectively. The $F_{1u}$ [$\nu_3$ (F-Si), $\nu_4$ (F-Si-F)] and the inactive $F_{2u}$ ($\nu_3$) modes become Infrared active in the site group, splitting each other into three components of $A_u$ symmetry. By crystal field effect (Davydov splitting effect), the *gerade* modes $A_g$ should split into two ($A_g$, $B_g$) active in Raman, and the *ungerade* $F_{1u}$ to two

Active-Infrared components ($A_u$, $B_u$), which gives 30 internal modes described in the factor group as [$6A_g$ (Ra) + $6B_g$ (Ra) + $9A_u$ (IR) + $9B_u$ (IR)]. The vibrational modes splitting is expected for $SiF_6^{2-}$ in the crystal by ($O_h \rightarrow C_i$) symmetry lowering.

**Table 3.** Correlation diagram of $SiF_6^{2-}$ internal vibrational modes in the crystal.

| Point symmetry ($O_h$) | Site symmetry ($C_i$) | Factor Group ($C_{2h}$) |
|---|---|---|
| $\nu_1$:1 $A_{1g}$ (Ra) | | |
| $\nu_2$:1 $E_g$ (Ra) | 6 $A_g$ (Ra) | 6 $A_g$ (Ra) |
| $\nu_5$: 1 $F_{2g}$ (Ra) | | 9 $A_u$ (IR) |
| $\nu_3$, $\nu_4$: 2 $F_{1u}$ (IR) | 9 $A_u$ (IR) | 6 $B_g$ (Ra) |
| $\nu_6$: 1 $F_{2u}$ (In) | | 9 $B_u$ (IR) |

3.3.3. Infrared and Raman spectra interpretation.

The Infrared and Raman spectra of $(N_2H_5)_2SiF_6$ are given in Figures 3 and 4, respectively. They are interpreted in terms of local symmetry $C_1$ for $N_2H_5^+$ cations (Table 2) and $C_i$ for $SiF_6^{2-}$ anions (Table 3). The bands' assignment (Table 4) is developed considering previous works on homologous salts [15,17, 18, 31-39]. Experimental and periodic DFT studies of infrared and Raman properties of the hexafluorosilicate compounds, $NH_3(CH_2)_4NH_3SiF_6$ (n=4, 6) were performed in crystal phase, where three-dimensional N-H···F hydrogen bonds (HB) network was formed [39].

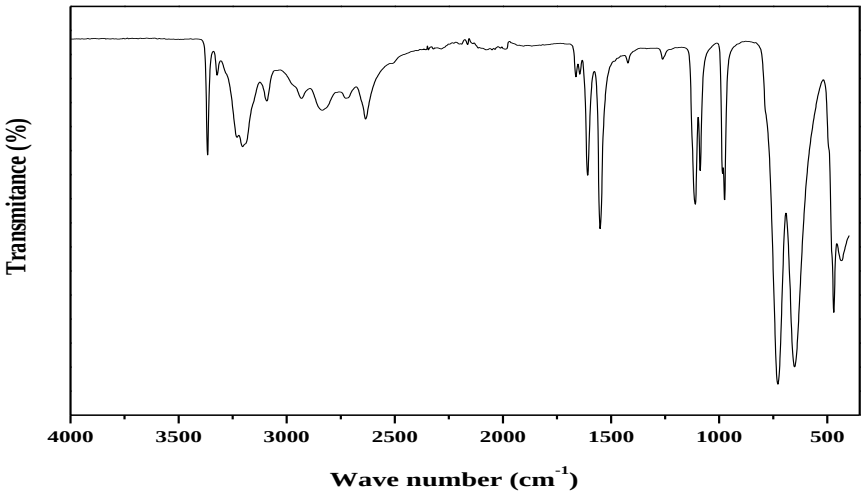


**Figure 3.** The infrared spectrum of $(N_2H_5)_2SiF_6$ recorded at room temperature in (450–4000) $cm^{-1}$.

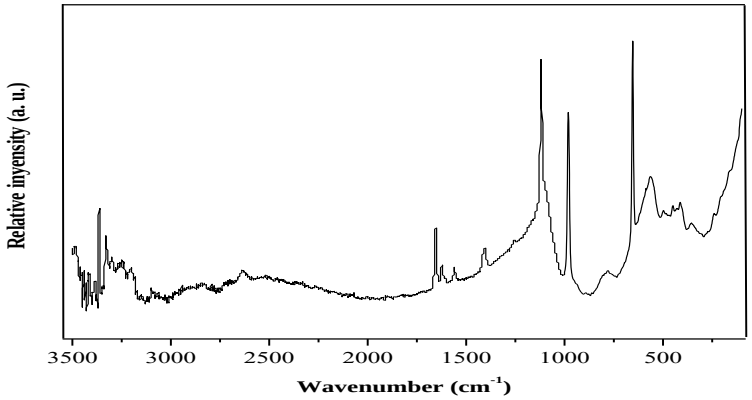


**Figure 4**. Raman spectrum of $(N_2H_5)_2SiF_6$ recorded at room temperature in (400–4000) $cm^{-1}$.

3.3.4. $N_2H_5^+$ cations modes.

The cationic bands are observed in (3300-2800 $cm^{-1}$) and (1664-974 $cm^{-1}$) frequency ranges. The Infrared (3300–2800 $cm^{-1}$) frequency range is due to N-H stretching modes. The two bands that appeared at 3368 and 3323 $cm^{-1}$ were assigned to anti-symmetric stretching modes $\nu_{as}$ ($NH_3$), which give weak to medium Raman bands at 3364, 3330, and 3299 $cm^{-1}$. The Infrared band observed at 3209 $cm^{-1}$, and the shoulder at 3235 $cm^{-1}$ was assigned to anti-symmetric stretching modes $\nu_{as}$ ($NH_2$); these modes appeared in the Raman spectrum as weak bands observed at 3263, 3248, 3238, 3228, 3202 $cm^{-1}$. The two weak bands observed at 3095 and 2928 $cm^{-1}$ were assigned to $\nu_s$ ($NH_3$) and $\nu_s$ ($NH_2$) symmetric stretching modes. The bands observed in the Infrared spectrum at 1664, 1613, and 1550 $cm^{-1}$ are all assigned to asymmetric $\delta_{as}(NH_3)/\delta_{as}(NH_2)$, and symmetric $\delta_s(NH_3)/\delta_s(NH_2)$ vibrations, respectively. These modes appeared in the Raman spectrum at 1654 as a medium band and weak bands at 1622 and 1559 $cm^{-1}$. The rooking r($NH_3$) and ν(N-N) vibrations are observed in the range (1259–780 $cm^{-1}$) as indicated in Table 3.

3.3.5. No fundamental vibration modes.

At lower wavenumbers of the NH stretching region of $(N_2H_5)_2SiF_6$ compound, three Infrared bands (2836, 2722, 2634 $cm^{-1}$) and one Raman band at 2638 $cm^{-1}$ were observed, which are due to overtone or combination bands of $NH_3$ bending modes as stated for hybrid compounds in literature [31, 36, 39]. These non-fundamental bands, intensified generally by the formation of appreciated hydrogen bonds, may be assigned as the following:

2836 $cm^{-1}$ (IR) ≈ 1550 + 1259 = 2809 $cm^{-1}$ = $\delta_s$ ($NH_3$)/ $\delta_s$ ($NH_2$) + r ($NH_3$)

2720 $cm^{-1}$ (IR) ≈ 1613 + 1113 = 2726 $cm^{-1}$ = $\delta_{as}$ ($NH_3$)/ $\delta_{as}$ ($NH_2$) + r($NH_3$)/ $\nu_{as}$ (N-N)

2634 $cm^{-1}$ (IR) ≈ 1550 + 1082 = 2632 $cm^{-1}$ = $\delta_s$ ($NH_3$)/ $\delta_s$ ($NH_2$) + r ($NH_3$)/ $\nu_s$ (N-N)

2638 $cm^{-1}$ (Ram) ≈ 1654 + 991 = 2645 $cm^{-1}$ = $\delta_{as}$ ($NH_3$)/ $\delta_{as}$ ($NH_2$) + r ($NH_3$)

3.3.6. $SiF_6^{2-}$ anions modes.

The vibrational spectra of alkylammonium hexafluorosilicate salts reported elsewhere [31-39] showed that $SiF_6^{2-}$ internal vibration modes anions appeared below 750 $cm^{-1}$. Indeed, the two Infrared bands observed at 726 and 651 $cm^{-1}$ are due to $F_{1u}$ [$\nu_3$ (F-Si)] vibration modes, while that observed at 474 and 435 $cm^{-1}$ are assigned to $F_{1u}$ [$\nu_4$ (F-Si-F)] vibrations modes. Gantar [20] assigned the Infrared bands observed at 638, 464, and 419 $cm^{-1}$ to the Raman active modes: $\nu_1$ (Si-F), $\nu_2$ (Si-F), and $\nu_5$ (F-Si-F), which are not infrared active in the $P2_1/n$ space group, as indicated by the theoretical group analysis (Table 2). The $SiF_6^{2-}$ anion vibration modes: $\nu_1$($\nu_s$ Si-F), $\nu_2$ ($\nu_{as}$ Si-F) and $\nu_5$ ($\delta_{as}$ F-Si-F) appeared generally in Raman spectra below 700 $cm^{-1}$. In the Raman spectrum of $(N_2H_5)_2SiF_6$ (Figure 3), the strong band observed at 655 $cm^{-1}$ is assigned to the $\nu_1$ ($\nu_s$ Si-F) modes of $A_g$ symmetry, while the weak peaks observed at 498 and 449 $cm^{-1}$ are assigned to the $\nu_2$ ($\nu_{as}$ Si-F) modes. The weak bands located at around 413 and 356 $cm^{-1}$ are assigned to $\nu_5$ ($\delta_{as}$ F-Si-F) bending modes.

**Table 4.** Assignment of the infrared bands of $(N_2H_5)_2SiF_6$ compound.

| Raman ($cm^{-1}$) | IR ($cm^{-1}$) | Assignment |
|---|---|---|
| 3488 m<br>3457 w<br>3440 w<br>3416 w | | |
| 3364 m<br>3330 m<br>3299 w | 3368 m<br>3323 w | $\nu_{as}$ ($NH_3$) |
| 3263 w<br>3248 w<br>3238 w<br>3228 w<br>3202 w, b | 3235 sh<br>3209 m | $\nu_{as}$ ($NH_2$) |
| | 3095 w | $\nu_s$ ($NH_3$) |
| | 2928 w | $\nu_s$ ($NH_2$) |
| 2638 w | 2836 w<br>2722 w<br>2634 m | Non-fundamental modes |
| 1654 m | 1664 w | $\delta_{as}$ ($NH_3$)/ $\delta_{as}$ ($NH_2$) |
| 1622 w | 1613 s | $\delta_{as}$ ($NH_3$)/ $\delta_{as}$ ($NH_2$) |
| 1559 w | 1550 s | $\delta_s$ ($NH_3$)/ $\delta_s$ ($NH_2$) |
| 1404 w | | |
| 1254 w | 1259 s | r ($NH_3$) |
| | 1113 s | r($NH_3$)/ $\nu_{as}$ (N-N) |
| | 1082 m | r ($NH_3$)/ $\nu_s$ (N-N) |
| 991 s | 974 s | r ($NH_3$) |
| 780 w | | r ($NH_3$) |
| | 726 vs | $\nu_3$ (Si-F) |
| 655 s | | $\nu_1$ ($\nu_s$ Si-F) |
| | 651 s | $\nu_3$ (Si-F) |
| 564 m, b | | |
| 498 w | | $\nu_2$ ($\nu_{as}$ Si-F) |
| | 474 m | $\nu_4$ (F-Si-F) |
| 449 w | | $\nu_2$ ($\nu_{as}$ Si-F) |
| | 435 w | $\nu_4$ (F-Si-F) |
| 413 w | | $\nu_5$ ($\delta_{as}$ F-Si-F) |
| 356 w | | $\nu_5$ ($\delta_{as}$ F-Si-F) |

*3.4. Electronic properties.*

Due to our laboratory's lack of apparatus measurements, we accomplished this investigation by calculating the optoelectronic based on the density functional theory implemented in the Wien2K code using the PBE-GGA approximation. The BoltzTrap code based on the semi-classical Boltzmann theory combined with the Wien2K package was used to compute the thermoelectric properties [27]. Figure 5 shows the direct band gap with a clear insulator behavior of the studied compound. We can notice that the maximum of the valence band (VB) and the minimum of the conduction band (CB) are located at the same point Γ, with a band gap energy value of about 7.04 eV. The calculated gap value is considered a strong band gap, implying that the compound may have low reactivity and good stability [40-43]. The strong energy gap of $(N_2H_5)_2SiF_6$ compound implied weak polarisability and low chemical reactivity, as found for other hexafluorosilicate salts.

*3.5. Optical properties.*

Optical properties were studied to investigate the inter-band transitions of double perovskites halides (DHPs) semiconductors for photovoltaic devices [44-46]. The optical properties of the $(N_2H_5)_2SiF_6$ compound are studied by figuring out the complex dielectric function ε (ω) [47], which includes a real and an imaginary part as represented in equation (1).

Optical conductivity, absorption spectra α(ω), reflectivity R(ω), and the refractive index n(ω) are investigated for the considered compound in the range between 100 nm and 1000 nm.

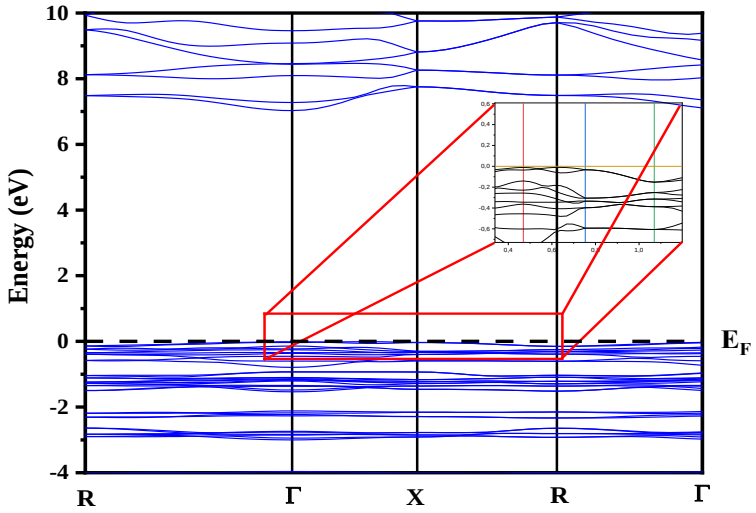


**Figure 5.** Band structure of $(N_2H_5)_2SiF_6$ compound.

$$\varepsilon(\omega) = \varepsilon_1(\omega) + i\,\varepsilon_2(\omega) \quad (1)$$

The imaginary part is described by [48]:

$$\varepsilon_2(\omega) = \frac{4\pi^2 e^2}{m^2\omega^2}\sum_{i,j}|< i|M|j >|^2 \times \left(f_i(1-f_i)\right)\delta\left(E_f - E_i - \hbar\omega\right)d^3k \quad (2)$$

In this equation, e is the charge of the electron, m is the mass, M is the transition moments elements, $f_i$ is Fermi's distribution function. The real part of the dielectric function $\varepsilon_1(\omega)$, can be obtained from the imaginary part $\varepsilon_2(\omega)$ using the Kramers-Kronig transformation:

$$\varepsilon_1(\omega) = 1 + \frac{2}{\pi}\int_0^{\infty}\frac{\varepsilon_2(\omega')\omega' d\omega'}{\omega'^2 - \omega^2} \quad (3)$$

The optical conductivity is represented in figure 6 depending on the wavelength between 100 nm and 1000 nm. We notice a high conductivity of the $(N_2H_5)_2SiF_6$ compound in the ultraviolet range. The optical conductivity exceeds 1000 $Ohm^{-1}$ $cm^{-1}$ in $\lambda < 100$ nm and decreases to zero for $\lambda > 200$ nm, implying high conductivity for high wavelength applications. We can see a slight difference between the [100] and the [001] direction (Figure 6), but they have the same behavior.

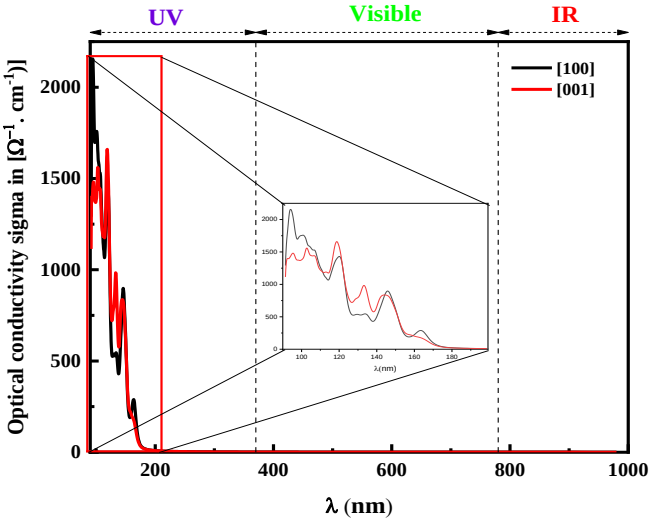


**Figure 6.** Optical conductivity of $(N_2H_5)_2SiF_6$ compound as a function of wavelength.

Absorption is a property that defines the conversion of light into energy. It depends on the electromagnetic frequency of the light and the object's nature of atoms. The absorption of light is, therefore, directly proportional to the frequency. For the studied compound, we can notice its high absorption coefficient reaching $50\times10^4$ $cm^{-1}$ in a small wavelength of the ultraviolet range, as seen in Figure 7, which makes this compound be used for optical applications in the UV region [49]. Besides, the compound showed low absorption coefficients in the visible spectrum, indicating that it can be used as a transparent system for solar cells [49]. There are compounds that are used in solar cells applications with a good quality of absorbance in the visible range ($22\times10^4$ $cm^{-1}$ at 7.2 eV), such as $(C_6H_{10}N_2)_2[Co(H_2O)_4P_2Mo_5O_{23}].6H_2O$ [50].

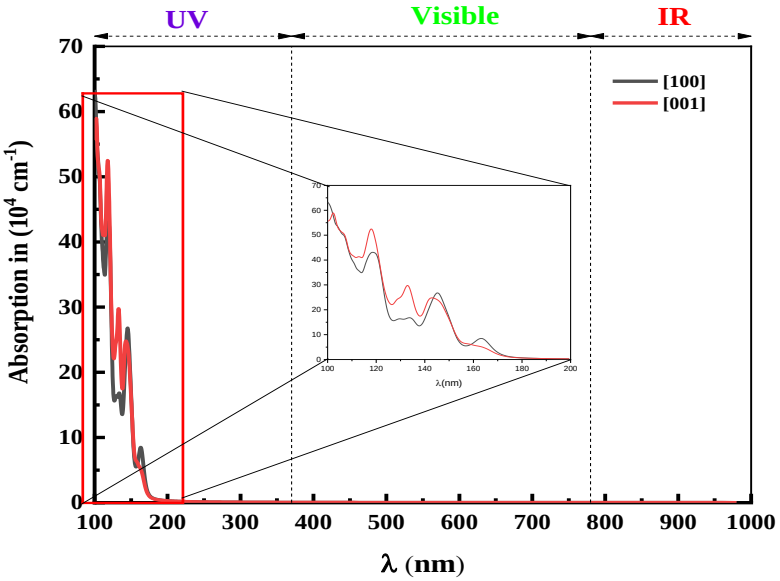


**Figure 7.** Absorption of $(N_2H_5)_2SiF_6$ compound as a function of wavelength.

The reflectivity of a material is its capacity to reflect a sample surface to the incident radiation flux. Figure 8 shows the reflectivity of the $(N_2H_5)_2SiF_6$ compound as a function of the wavelength of the spectra; we can notice fluctuation between 1% and 5% in the range between 100 and 200 nm. After that, we have a stability of a low reflectivity value for $\lambda < 200$ nm in the ultraviolet region.

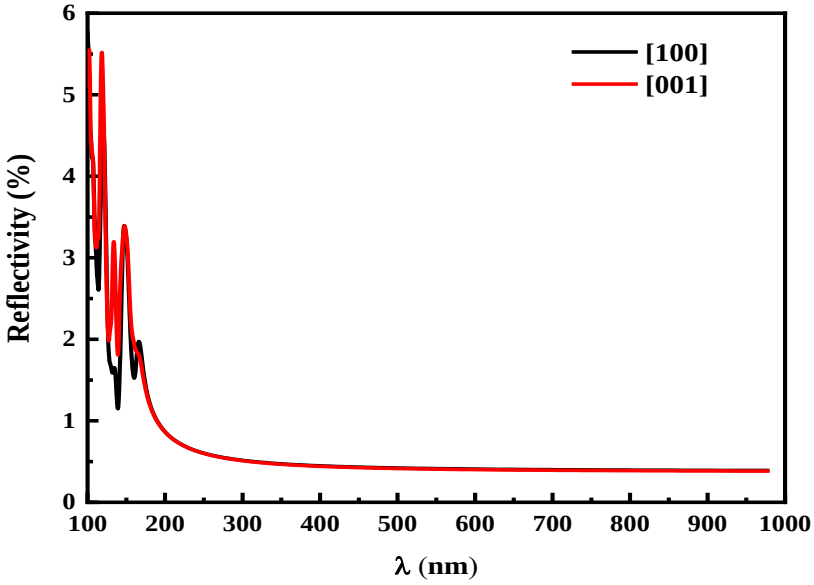


**Figure 8.** The reflectivity of the $(N_2H_5)_2SiF_6$ compound as a function of wavelength.

In optics, the refraction index of a material is a dimensionless number that describes how fast light travels through the material. Figure 9 represents the refraction index in the range between 100 nm and 1000 nm for the $(N_2H_5)_2SiF_6$ compound. It varied between 1 and 1.4 for the wavelength between 100 and 200 nm and stabilized at the average of 1.2 for $\lambda > 200$ nm.

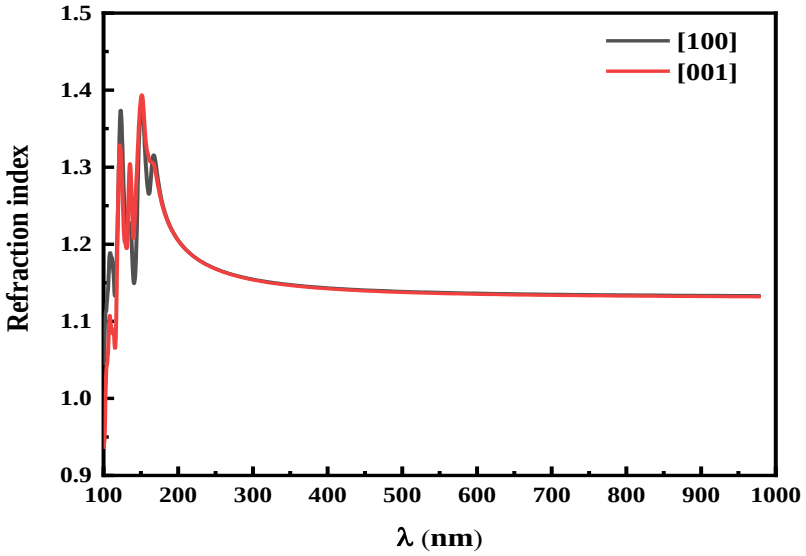


**Figure 9.** Refractivity index of the $(N_2H_5)_2SiF_6$ compound as a function of wavelength.

*3.6. Photocatalytic properties.*

A photocatalytic properties investigation requires studying the optical band gap, the potentials of valence band maxima (VBM), and the relative effective mass ratio (D) of photogenerated electrons and holes. The potentials of valence band maxima (VBM) and the conduction band minima (CBM), play important roles in the redox reactions in the electrolyte system [51]. The well-known Mulliken electronegativity theory identifies the band-edge potential levels of (N2H5)2SiF6 photocatalysis [52]. The value of valence band maxima (VB) and conduction band minima (CB) energies can be calculated using the equations:

$$E_{VB} = \chi - E_0 + 0.5\, E_g \quad (4)$$

$$E_{CB} = E_{VB} - E_g \quad (5)$$

where $E_{VB}$ and $E_{CB}$ are the valence band and the conduction band edge potential, respectively. $E_0$ is the energy of free electrons on the hydrogen scale ($E_0$=4.5 eV) [51]. $\chi$ is the absolute electronegativity of the studied compound ($\chi = 8.2$), which is calculated using the following equation:

$$\chi\,((N_2H_5)_2SiF_6) = (\chi(N)^4\,\chi(H)^{10}\,\chi(Si)\,\chi(F)^6\,)^{1/21} \quad (6)$$

where $\chi(N)$, $\chi(H)$, $\chi(Si)$, and $\chi(F)$ are the absolute electronegativity of N, H, Si, and F elements, which take values of 6.97, 7.97, 3.60, and 11.00, respectively [53]. The band gap energy of $(N_2H_5)_2SiF_6$ is 7.04 eV. The photocatalytic reaction mechanism is shown in Figure 10. The electrons gain energy when the incident photon is equal to or greater than the bandgap of (N2H5)2SiF6. As a result, these electrons transfer from the valence band (VB) to the conduction one (CB), generating holes ($h^+$) in the VB and electrons ($e^-$) in the CB. According to the NHE (normal hydrogen electrode), the CB and the VB edge potentials of $(N_2H_5)_2SiF_6$ are 0.18 and 7.22, respectively. Consequently, the photoinduced holes in the valence band can oxidize water ($H_2O$) and generate hydroxyl radicals $O_2$, $H_2O_2$, and $O_3$. These radicals are able

to reduce, decompose, and/or remediate organic pollutants [54–55], dye molecules [56], and dyes [57–58] under solar UV-light irradiation. The photocatalytic mechanism of the studied compound can be described as follow:

$$4\mathrm{H}^+ + O_2 + 4e^- \rightarrow 2H_2O \quad (7)$$

$$H_2O_2 + 2\mathrm{H}^+ + 2e^- \rightarrow 2H_2O \quad (8)$$

$$O_3 + 2\mathrm{H}^+ + 2e^- \rightarrow O_2 + H_2O \quad (9)$$

The effective mass values of photoinduced electrons ($m_h^*(\mathrm{m}_0)$) and holes ($m_e^*(\mathrm{m}_0)$) are 247.85 $\mathrm{m}_0$ and 104.67 $\mathrm{m}_0$, respectively. The calculated electron effective mass is much higher than the hole effective mass. This suggests that holes have a higher chance to participate in the photocatalytic process, signifying the large band gap of $(N_2H_5)_2SiF_6$, as found elsewhere for other hexafluorosilicate compounds [40, 41]. This fact is explained by the slower diffusion rates, which make the separation of electron-hole pairs more difficult [57]. The calculated relative ratio of effective masses is about 0.42. This parameter was calculated to estimate the charge separation efficiency [59]. The relative ratio (D) of the effective masses, which play a significant role in photocatalysis, is evaluated via the following formula:

$$\mathrm{D} = m_h^*(\mathrm{m}_0) / m_e^*(\mathrm{m}_0) \quad (10)$$

Generally, a higher D value signifies a higher probability of photoinduced electron-hole pairs separation, thereby, a lower recombination rate to boost the photocatalytic activity.

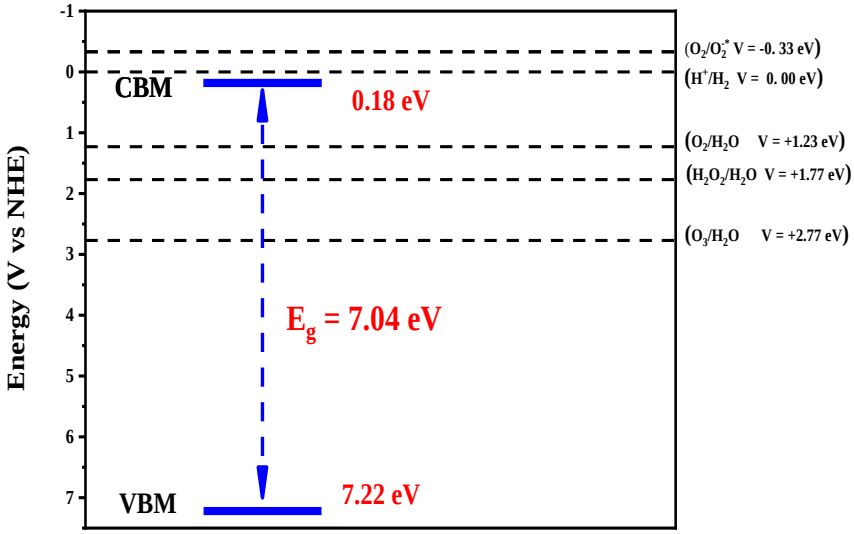


**Figure 10.** Schematic illustration for the calculated energy band diagram of $(N_2H_5)_2SiF_6$.

The D value is lesser than one, indicating that the recombination rate is higher, which impedes its photocatalytic properties [60], then the improvement of this property requires a reduction of the band gap of this compound by impurities doping [61–62], or heterojunction process [63].

*3.7. Transport properties.*

The conversion of waste heat into electricity via the thermoelectrical effect remains one of the most important sources worldwide. Therefore, the efficiency of this application is evaluated through the calculation of the figure of merit (*ZT*) and power factor (*PF*). The characteristic parameters of the transport properties include electrical conductivity, thermal

conductivity, Seebeck coefficient, carrier mobility, and carrier concentration of the studied compound, which have been investigated at room temperature via the BoltzTrap package and recapitulated in Table 4.

**Table 4.** Transport properties calculated at an ambient temperature of $(N_2H_5)_2SiF_6$.

| **σ (S.cm$^{-1}$.s$^{-1}$)/ τ** | **2.04 10$^{18}$** |
|---|---|
| $K_{el}$ (W.m$^{-1}$.K$^{-1}$.s$^{-1}$)/ τ | 2.81 10$^{13}$ |
| S (V.K$^{-1}$) | 1.67 10$^{-4}$ |
| $\mu_p$ (cm$^2$.V$^{-1}$.s$^{-1}$) | 1.07 10$^{17}$ |
| p (cm$^{-3}$) | 6.98 10$^{23}$ |
| ZT | 0.61 |
| PF (W. cm$^{-1}$ K$^{-2}$) | 5.67 10$^{10}$ |

The temperature depends on the figure of merit ZT has been calculated using the following equation:

$$ZT = \frac{\sigma S^2 T}{\kappa} \quad (11)$$

where σ, S, k, and T are the electrical conductivity, thermal conductivity, Seebeck coefficient, and temperature, respectively. Besides, the variation of power factor as a function of temperature is calculated as follows:

$$PF = \sigma S^2 \quad (12)$$

From Table 4, we can notice the high electrical conductivity (2.04 10$^{18}$ S.cm$^{-1}$.s$^{-1}$), high thermal conductivity (2.81 10$^{13}$ W.m$^{-1}$.K$^{-1}$.s$^{-1}$), low and positive Seebeck coefficient (1.67 10$^{-4}$ V.K$^{-1}$) of $(N_2H_5)_2SiF_6$. The Seebeck coefficient's positive sign signifies that holes' contribution is more important than electrons in this material. This result is proved before via the calculation of the carrier's effective masses. At the same time, it has a higher power factor value due to the higher electrical conductivity value. The lower value of the figure of merit. The simulated compound possesses a value of the figure of merit less than a unit due to the low Seebeck coefficient and the high thermal conductivity. Hence, allowing the impendence of the performance of the conversion of the waste heat into electricity. In this case, it is necessary to improve the electrical conductivity of this compound in order to increase the value of the figure of merit.

## 4. Conclusions

The $(N_2H_5)_2SiF_6$ compound was reinvestigated using the XRD, Infrared-Raman spectroscopy techniques to complete the study made elsewhere [20, 21]. Its crystal structure at ambient temperature (Monoclinic, $P2_1/n$, Z=2) is built by zigzag chains $N_2H_5^+$ cations running along [0 1 0] direction and slightly distorted $SiF_6^{2-}$ octahedron anions parallel to [1 0 0] direction. The anions and cations were linked via N-H***F hydrogen bonds (2.02 -2.52 Å). The Infrared R (450–4000 cm$^{-1}$) and Raman (50–3500 cm$^{-1}$) spectra recorded at room temperature were interpreted based on factor group analysis, predicting the type, number, and symmetry of the normal modes of the title compound. This allowed us to propose a rigorous assignment of anionic vibration modes and discuss that made elsewhere. Besides, the vibrational spectra confirm the presence of appreciated hydrogen bonds N-H***F, traduced by the appearance of non-fundamental bands at lower frequencies of the N-H stretching region.

In addition, the electronic structure, optical, photocatalytic, and thermoelectric properties of $(N_2H_5)_2SiF_6$ are investigated using the full-potential linearized augmented plane wave (FP-LAPW) method, using the generalized gradient approximation (GGA). So, the photocatalytic reaction mechanism is described for this compound, with direct band gap energy (7.04 eV) at point Γ. The optical properties (absorption, conductivity, reflectivity, and refractivity index) were evaluated in the wavelength range (100-1000 nm). The high absorption coefficient ($50\times10^4$ $cm^{-1}$) in the ultraviolet range, the very high optical conductivity (zero for $\lambda > 200$ nm) for high wavelength applications, the high electrical (2.04 $10^{18}$ $S.cm^{-1}.s^{-1}$) and thermal (2.81 $10^{13}$ $W.m^{-1}.K^{-1}.s^{-1}$) conductivities propose the $(N_2H_5)_2SiF_6$ as a perspective material in different applications.

## Funding

This research received no external funding.

## Conflicts of Interest

The authors declare no conflict of interest.

## References

1. Braieka, F.; Elleuchb, S.; Marzouki, R.; Graia, M. Experimental and theoretical studies of the structural, vibrational and optical properties of a new hybrid material $(C_5H_6N_2Cl)_2SiF_6$,. *J. Molecular Structure* **2021**, *1232*, 129990, https://doi.org/10.1016/j.molstruc.2021.129990. .
2. Jonathan, L.; Diguna, L.J.; Samy, O.; Muqoyyanah, M.; Abu Bakar, S.; Birowosuto, M.D.; El Moutaouakil, A. Hybrid Organic–Inorganic Perovskite Halide Materials for Photovoltaics towards Their Commercialization. *J. Polymers* **2022**, *14*, 1059, https://doi.org/10.3390/polym14051059.
3. Zhang, Y.; Kirs, A.; Ambroz, F.; Lin, C.-T.; Bati, A.S.R.; Parkin, I.P.; Shapter, J.G.; Batmunkh, M.; Macdonald, T.J. Ambient Fabrication of Organic–Inorganic Hybrid Perovskite Solar Cells. *J. Small Methods* **2021**, *5*, 2000744, https://doi.org/10.1002/smtd.202000744.
4. Wang, M.; Wang, W.; Ma, B.; Shen, W.; Liu, L.; Cao, K.; Chen, S.; Huang, W. Lead-Free Perovskite Materials for Solar Cells. *J. Nano-Micro Lett.* **2021**, *13*, 62. https://doi.org/10.1007/s40820-020-00578-z.
5. Lim, A.R.; Park, S.H. Characterization on Lead-Free Hybrid Perovskite $[NH_3(CH_2)_5NH_3]CuCl_4$: Thermodynamic Properties and Molecular Dynamics. *J. Molecules* **2022**, *27*, 4546, https://doi.org/10.3390%2Fmolecules27144546.
6. Abdel-Aal, S.K.; Ouasri, A. Crystal structures, Hirshfield surfaces analysis, Infrared and Raman studies of organic-inorganic hybrid perovskite salts $NH_3(CH_2)_nNH_3MnCl_4$ (n = 5, 6). *J. Solid State Chemistry* **2022**, *314*, 123401, https://doi.org/10.1016/j.jssc.2022.123401.
7. Abdel-Aal, S.K.; Ouasri, A. Crystal Structure, Hirshfeld surfaces, Infrared-Raman spectra of tetrachlorocobaltate salts $NH_3(CH_2)_nNH_3CoCl_4$ (n=4, 9). *J. Molecular structure* **2022**, *1251*, 131997, https://doi.org/10.1016/j.molstruc.2021.131997.
8. Pravan, O.; Viswesh P.; Devadas B.P. A Review of 2D Perovskites and Carbon-Based Nanomaterials for Applications in Solar Cells and Photodetectors. *ECS Journal of Solid State Science and Technology* **2021**, *10*, 031009, https://iopscience.iop.org/article/10.1149/2162-8777/abefaf/meta.
9. Hamdi, I.; Yeasin Khan, Y.; Aouaini, F.; Seo, J.H.; Hyun-Joo Koo, H.-J.; Turnbull, Mark M; Walker, W.; Naïli, H. A copper-based 2D hybrid perovskite solar absorber as a potential eco-friendly alternative to lead halide perovskites†. *J. Materials Chemistry C* **2022**, *10*, 3738-3745, https://doi.org/10.1039/D1TC05047H.
10. Kojic-Prodic, B.; Matkovic, B.; Scavnicar, S. The crystal structure of hydrazinium(+2) hexa-fluorotitanate(IV), $N_2H_6TiF_6$. *J. Acta Cryst.* **1971**, *B27*, 635-637, https://doi.org/10.1107/S0567740871002681.
11. Kojic-Prodic, B.; Scavnicar, S.; Matkovic, B. The crystal structure of hydrazinium(+2) hexafluorozirconate, $N_2H_6ZrF_6$. *J. Acta Cryst.* **1971**, *B27*, 638-644, https://doi.org/10.1016/S0022-1139(00)81034-9.
12. Frlec, B. ; Gantar, D.; Golic, L.; Leban, I. Hydrazinium(2+) hexafluorosilicate(IV). *J. Acta Cryst.* **1980**, *B36*, 1917-1918., https://doi.org/10.1107/S0567740880007455.

13. Golic, L.; Kauclic, V.; Kojic-Prodic, B. Hydrazinium(2+) difluoride hexafluorotitanate(IV). *J. Acta Cryst*. **1980**, *B36*, 659-661, https://doi.org/10.1107/S0567740880004025.
14. Cameron, T.S.; Knop, O.; MacDonald, L.A. Hydrazonium (2+) hexafluorosilicate, $N_2H_6SiF_6$: a NaCl-type structure with two-dimensional hydrogen-bonding networks. *Can. J. Chem*. **1983**, *61*, 184-188., https://doi.org/10.1139/v83-032.
15. Ouasri, A.; Rhandour, A.; Dhamelincourt, M.-C; Dhamelincourt, P.; Mazzah, A. Structural and vibrational study of the hydrazinium hexafluorosilicate. *J. Raman Spectroscopy* **2002**, *33*, 726-729, https://doi.org/10.1002/jrs.908.
16. Leban, I.; Jesih, A.; Rahten. Hydrazinium (1+) hexafluorotitanate(IV), $2N_2H_5^+.TiF_6^{2-}$. *J. Acta Cryst.* **1994**, *C50*, 842-843, https://doi.org/10.1107/S0108270193011795.
17. Gantar, O.; Rahten, A.; Volvasek, B. Thermal behaviour of new hydrazinium(l+) hexafluorozirconate and -hafnate. *J. Fluor. Chem.* **1988**, *42*, 335-344, https://doi.org/10.1016/0040-6031(86)85086-9.
18. Gantar, O.; Golic, L.; Leban, I.; Rahten, A. Hydrazinium(1+) hexafluorogermanate(IV) and hydrazinium(2+) hexafluorogermanate(IV) difluoride. *J. Fluor. Chem*. **1985**, *30*, 19-28, https://doi.org/10.1016/S0022-1139(00)80519-9.
19. Gantar, D; Rahten. A. Synthesis and Characterization of $(N_2H_5)_2SiF_6$ (I) and thermal analysis of $(N_2H_5)_2SiF_6$ and $N_2H_6SiF_6$(II). *J. ChemInform*. **1987**, *18*, https://doi.org/10.1002/chin.198709033.
20. Gantar, D.; Rahten, A. Synthesis and characterization of $(N_2H_5)_2SiF_6$ and thermal analysis of $(N_2H_5)_2SiF_6$ and $N_2H_6SiF_6$, . *J. Thermochim. Acta* **1986**, *108*, 149-155, https://doi.org/10.1016/0040-6031(86)85086-9.
21. Ouasri, A.; Lambarki, F.; Rhandour, A.; Saadi, M.; El- Ammari, L. Crystal structure and Hirshfeld analysis of bis [hydrazinium (1+)] hexafluorosilicate: $(N_2H_5)_2SiF_6$. *J. Acta Cryst.* **2019**, *E75*, 1507-1510, https://doi.org/10.1107/s2056989019012672.
22. El hajri, F., Benzekri, Z.; Sibous, S.; Ouasri, A.; Boukhris, S.; Hassikou, A.; Rhandour, A.; Souizi, A. Bis [hydrazinium (1+)] hexafluoridosilicate: $(N_2H_5)_2SiF_6$ novel hybrid crystal as an efficient, reusable and environmentally friendly heterogeneous catalyst for knoevenagel condensation and synthesis of Biscoumarine derivatives. *J. Mol. Struct*. **2021**, *1230*, 129890, https://doi.org/10.1016/j.molstruc.2021.129890.
23. El hajri, F.; Benzekri, Z.; Anahmadi, H.; Sibous, S.; Ouasri, A.; Souizi, A.; Hassikou, A.; Rhandour, A.; Boukhris, S.; *Investigation of catalytic performance of Bis [hydrazinium (1+)] hexafluoridosilicate: $(N_2H_5)_2SiF_6$ in synthesis of 2,4,5-triaryl*-1H-*imidazoles and 2,3-dihydroquinazolin-4 (*1H*)-ones under Green conditions*. *J. Inorg. Chim. Acta* **2022**, *536*, 120915, https://doi.org/10.1016/j.ica.2022.120915.
24. Petersen, M. ; Wagner, F. ; Hufnagel, L. ; Scheffler, M.; Blaha, P.; Schwarz, K. Improving the efficiency of FP-LAPW calculations. *J. Comput. Phys. Commun*. **2000**, *126*, 294–309, https://doi.org/10.1016/S0010-4655(99)00495-6.
25. Schwarz, K.; Blaha, P.; Madsen, G.K.H. Electronic structure calculations of solids using the WIEN2k package for material sciences. *J. Comput. Phys. Commun*. **2002**, *147*, 71–76, https://doi.org/10.1016/S0010-4655(02)00206-0.
26. Perdew, J.P. ; Yue, W. Accurate and simple density functional for the electronic exchange energy: Generalized gradient approximation. *J. Phys. Rev. B* **1986**, *33*, 8800–8802, https://doi.org/10.1103/physrevb.33.8800.
27. Madsen, G.K.H.; Singh, D.J. BoltzTraP. A code for calculating band-structure dependent quantities. *J. Comput. Phys. Commun*. **2006,** *175*, 67–71, https://doi.org/10.1016/j.cpc.2006.03.007.
28. Ertl, A.; Hughes, J.M.; Pertlik, F.; Foit, JR.F.F.; Wright, S.E. ; Brandstatter, F.; Marler, B. Polyhedron distortions in tourmaline. *The Canadian Mineralogist* **2002**, *40*, 153-162, https://doi.org/10.2113/gscanmin.40.1.153.
29. Ouasri, A.; Rhandour, A.; Saadi, M.; El Ammari, L. Crystal structure, powder X-Ray diffraction, Hirshfeld, DFT, thermal and Infrared-Raman studies, and symmetry analysis of the relationship between the novel tetragonal $[(CH_3)_4N]_2SiF_6$ and the Fm3m cubic antifluorite structure. *J. Mol. Struct.* **2022**, *1248*, 131455, https://doi.org/10.1016/j.molstruc.2021.131455.
30. Ouasri, A.; Rhandour, A. Structural, vibrational, thermal, phase transitions, and properties of alkylammonium and alkylenediammonium hexafluorosilicates. *Rus. J. Coord. Chem*. **2021**, *47*, 502-517, https://link.springer.com/article/10.1134/S1070328421070046.
31. Ouasri, A.; Rhandour, A.; Dhamelincourt, M.C.; Dhamelincourt, P.; Mazzah, A. Vibrational study of $(CH_3)_4NSbCl_6$ and $[(CH_3)_4N]_2SiF_6$,. *J. Spectrochim. Acta A* **2002**, *58*, 2779-2788, https://doi.org/10.1016/s1386-1425(02)00019-7.

32. Ouasri, A.; Rhandour, A.; Dhamelincourt, M.C.; Dhamelincourt, P.; Mazzah, A.; Taibi, M. Infrared and dielectric studies of $[(C_2H_5)_4N]_2SiF_6$. *J. Phase trans*. **2003**, *76*, 701-709, https://doi.org/10.1080/0141159021000037240.
33. Ouasri, A.; Rhandour, A.; Dhamelincourt, M.C.; Dhamelincourt, P.; Mazzah, A.; Taibi, M. Structural phase transitions in $[(C_2H_5)_4N]_2SiF_6$; Differential scanning calorimetry and Raman studies. *J. Ram. Spectrosc*. **2002**, *33*, 715-719, https://doi.org/10.1002/jrs.902.
34. Ouasri, A.; Rhandour, A.; Dhamelincourt, M.C.; Dhamelincourt, P.; Mazzah, A. The infrared and Raman spectra of ethylammonium hexafluorosilicate $[C_2H_5NH_3]_2SiF_6$. *J. Spectrochim. Acta A* **2003**, *59*, 357-362, https://doi.org/10.1016/s1386-1425(02)00165-8.
35. Ouasri, A.; Rhandour, A.; Dhamelincourt, M.C.; Dhamelincourt, P.; Mazzah, A. Structure and vibrational study of the trimethylammonium hexafluorosilicate $[(CH_3)_3NH]_2SiF_6$ compound. *J. Spectrochim. Acta A* **2003**, *59*, 851-857, https://doi.org/10.1016/S1386-1425(02)00231-7.
36. Jeghnou, H.; Ouasri, A.; Rhandour, A.; Dhamelincourt, M.C; Dhamelincourt, P.; Mazzah, A. Structural phase transition in $[C_4H_9NH_3]_2SiF_6$: DSC and Raman studies. *J. Ram. Spectrosc*. **2003**, *34*, 126-130, https://doi.org/10.1002/jrs.964.
37. Jeghnou, H.; Ouasri, A.; Rhandour, A.; Dhamelincourt, M.C; Dhamelincourt, P.; Mazzah, A. Structural phase transition in $[C_6H_5NH_3]_2SiF_6$, DSC and Raman studies. *J. Ram. Spectrosc*. **2003**, *34*, 399-403, https://doi.org/10.1002/jrs.1008.
38. Jeghnou, H.; Ouasri, A.; Rhandour, A.; Dhamelincourt, M.C; Dhamelincourt, P.; Mazzah, A. Differential scanning calorimetric and Raman studies of a phase transition in $[C_3H_7NH_3]_2SiF_6$. *J. Ram. Spectrosc.* **2004**, *35*, 261-265, https://doi.org/10.1002/jrs.1145.
39. Ouasri, A.; Lambarki, F.; Rhandour, A.; K. Zahariev, Ts.; Trendafilova, N.; Georgieva I. Solid state DFT modeling and vibrational characterisation of butylenediammonium and hexylenediammonium hexafluorosilicate $NH_3(CH_2)_nNH_3SiF_6$ (n=4, 6). *J. Vib. Spectrosc*. **2017**, *88C*, 83-93, https://doi.org/10.1016/j.vibspec.2016.11.006.
40. Jalbout, A.F.; Jiang, Z.Y.; Ouasri, A.; Jeghnou, H.; Rhandour, A.; Dhamelincourt, M.C.; Dhamelincourt, P.; Mazzah. A. Theoretical and experimental analysis of $[C_6H_5NH_3]_2SiF_6$. *J. Vib. Spectrosc*. **2003**, *33*, 21-30, https://doi.org/10.1016/S0924-2031(03)00067-5.
41. Jalbout, A.F.; Ouasri, A.; Jeghnou, H.; Rhandour, A. Experimental and theoretical studies of monoalkylammoniums hexafluorosilicate $[CH_3(CH_2)_nNH_3]_2SiF_6$ (n = 2, 3) and diethylammonium hexafluorosilicate $[(C_2H_5)_2NH_2]_2SiF_6$. *J. Vibr. Spectrosc*. **2007**, *44*, 94 -100, http://dx.doi.org/10.1016/j.vibspec.2006.09.006.
42. Ouasri, A.; El-Adel, L.; Zouihri, H.; Rhandour, A.; Jalbout, A.F. TGA, Hirshfeld, computational and Raman spectroscopy studies of diethylammonium hexachloroplumbate $[(C_2H_5)_2NH_2]_2PbCl_6$ (IV). *J. Mol. Struct*. **2018**, *1157*, 621-630, https://doi.org/10.1016/j.molstruc.2017.12.093.
43. El Makhloufy, S.; Belhabra, B.; Zeraf, S.; Ouasri, A.; Chtita, S.; Saadi, M.: El Ammari, L.; Belaaouad, S. Synthesis, Crystal Structure, IR spectroscopy, and DFT computation of 2-carboxyanilinium dihydrogen phosphate ($C_7H_8NO_2^+.H_2PO_4^-$). *J. Molecular Structure*, **2021**, *1242*, 130707, https://doi.org/10.1016/j.molstruc.2021.130707.
44. Dahbi, S.; Tahiri, N.; El Bounagui, O.; Ez-Zahraouy, H. Chalcogens' impurities and a single F-center in perovskite $SrHfO_3$ compound: Ab initio calculations. *J. Materials Science in Semiconductor Processing* **2022**, *138*, 106271, https://doi.org/10.1016/j.mssp.2021.106271.
45. Dahbi, S.; Tahiri, N.; El Bounagui, O.; Ez-Zahraouy, H. Calcium hafnate perovskite from an insulator to a semiconductor for photovoltaic and photocatalytic hydrogen production from water splitting applications. *J. Superlattices and Microstructures* **2021**, *160*, 107058, https://doi.org/10.1016/j.spmi.2021.107058.
46. Dahbi, S.; Tahiri, N.; El Bounagui, O.; Ez-Zahraouy, H. Electronic, optical, and thermoelectric properties of perovskite $BaTiO_3$ compound under the effect of compressive strain. *J. Chem. Phys*. **2021**, *544*, 111105, https://doi.org/10.1016/j.chemphys.2021.111105.
47. Cui, S. ; Feng, W.; Hu, H. ; Feng, Z.; Wang. Y. High-pressure structural, electronic and optical properties of $KMgF_3$: A first-principles study. *J. Alloys and Comp*. **2009**, *484*, 597-600, https://doi.org/10.1016/j.jallcom.2009.05.005.
48. Hamideddine, I.; Tahiri, N.; El Bounagui, O. ; Ez-Zahraouy, H. Theoretical investigation of electronic and optical properties of the CuIn1-x $GaxSe_2$: Ab initio calculation. *J. Optik* **2020**, *207*, 163881, https://doi.org/10.1016/j.ijleo.2019.163881.

49. Dahbi, S.; Tahiri, N.; El Bounagui, O.; Ez-Zahraouy, H. Importance of spin-orbit coupling on photovoltaic properties of Pb-free vacancy ordered double perovskites halides $X_2TeY_6$ (X = Cs, Rb, and Y = I, Br, Cl): Firstprinciples calculation. *International Journal of Energy Research* **2022**., *46*, 8433-8442, https://doi.org/10.1002/er.7631.
50. Baaalla, N.; Ammari, Y; Hlil, E.K; Abid, S.; Masrour, R.; Benyoussef A.; El Kenz, A. The novel material based on strandberg-type hybrid complex $(C_6H_{10}N_2)_2[Co(H_2O)_4P_2Mo_5O_{23}].6H_2O$: Experimental and simulations investigation on electronic, optical, and magnetocaloric properties. *J. Ceramics International* **2021**, *47*, 2338-2346, https://doi.org/10.1016/j.ceramint.2020.09.076.
51. Basith, M.A.; Ahsan, R.; Zarin, I.; Jalil, M.A. Enhanced photocatalytic dye degradation and hydrogen production ability of $Bi_{25}FeO_{40}$-rGO nanocomposite and mechanism insight. *J. Sci. Rep*. **2018,** *8*, 11090, https://www.nature.com/articles/s41598-018-29402-w.
52. Wang G. et al., Enhanced visible-light responsive photocatalytic activity of $Bi_{25}FeO_{40}/Bi_2Fe_4O_9$ composites and mechanism investigation. *J. Mater. Sci. Mater. Electron*. **2019**, *30*, 10923-10933, https://link.springer.com/article/10.1007/s10854-019-01436-4.
53. Tantardini, C.; Oganov, A.R. Thermochemical electronegativities of the elements. *J. Nat. Commun.* **2021**, *12*, 2087, https://www.nature.com/articles/s41467-021-22429-0.
54. Huang, Y. ; Nengzi, L. ; Li, X.; Meng, L.; Song, Q.; Cheng, X. Fabrication of $Cu_2O/Bi_{25}FeO_{40}$ nanocomposite and its enhanced photocatalytic mechanism and degradation pathways of sulfamethoxazole. *J. Mater. Sci. Semicond. Process* **2020**, *109*, 104932, https://doi.org/10.1016/j.mssp.2020.104932.
55. Sun, A.; Chen, H.; Song, C.; Jiang, F.; Wang, X.; Fu, Y. Magnetic $Bi_{25}FeO_{40}$-graphene catalyst and its high visible-light photocatalytic performance. *J. RSC Adv.* **2013**, *3*, 4332, https://pubs.rsc.org/en/content/articlelanding/2013/ra/c3ra22626c.
56. Kalikeri, S.; Shetty Kodialbail, V. Solar light-driven photocatalysis using mixed-phase bismuth ferrite ($BiFeO_3/Bi_{25}FeO_{40}$) nanoparticles for remediation of dye-contaminated water: kinetics and comparison with artificial UV and visible light-mediated photocatalysis. *J. Environ. Sci. Pollut. Res*. **2018**, *25*, 13881–13893, https://link.springer.com/article/10.1007/s11356-018-1291-0.
57. Ren, L.; Lu, S.Y.; Fang, J.Z.; Wu, Y. ; Chen, D.Z.; Huang, L.Y. ; Chen, Y.F.; Cheng, C.; Liang, Y.; Fang, Z.Q. Enhanced degradation of organic pollutants using $Bi_{25}FeO_{40}$ microcrystals as an efficient reusable heterogeneous photo-Fenton like catalyst. *J. Catal. Today* **2017**, *281*, 656–661, https://doi.org/10.1016/j.cattod.2016.06.028.
58. Zhang, C.Y.; Sun, H.J. ; Chen, W.; Zhou, J. ; Li, B.; Wang, Y.B. Hydrothermal synthesis and photocatalyticProperty of $Bi_{25}FeO_{40}$ powders', in 2009 18th IEEE International Symposium on the Applications of Ferroelectrics. *Xian, China* **2009**, 1–3, https://ieeexplore.ieee.org/document/5307531.
59. Opoku, F.; Govender, K.K.; van Sittert, C.G.C.E.; Govender, P.P. Enhancing Charge Separation and Photocatalytic Activity of Cubic $SrTiO_3$ with Perovskite-Type Materials $MTaO_3$ (M=Na, K) for Environmental Remediation: A First-Principles Study. *J. Chem. Select*. **2017**, *2*, 6304–6316, https://doi.org/10.1002/slct.201700886.
60. Arunachalam, P. ; Nagai, K. ; Amer, M.S.; Ghanem, M.A.; Ramalingam, R.J.; Al-Mayouf, A.M. Recent Developments in the Use of Heterogeneous Semiconductor Photocatalyst Based Materials for a Visible-Light-Induced Water-Splitting System-A Brief Review. *J. Catalysts* **2021**, *11*, 160, https://doi.org/10.3390/catal11020160.
61. Xing, Y.; Wang, X.; Hao, S.; Zhang, X.; Wang, X.; Ma, W.; Zhao, G. ; Xu, X. Recent advances in the improvement of $g\text{-}C_3N_4$ based photocatalytic materials. *J. Chin. Chem. Lett.* **2021**, *32*, 13-20, https://doi.org/10.1016/j.cclet.2020.11.011.
62. Habib I.Y. ; Burhan, J.; Jaladi, F.; Lim, C.M.; Usman, A.; Kumara, N.T.R.N.; Mahadi, A.H. Effect of Cr doping in $CeO_2$ nanostructures on photocatalysis and $H_2O_2$ assisted methylene blue dye degradation. *J. Catal. Today* **2021**, *375*, 506–513, https://doi.org/10.1016/j.cattod.2020.04.008.
63. Lai, C.; Xu, F.; Zhang, M.; Li, B.; Liu, S.; Yi, H.; Li, L.; Qin, L.; Liu, X.; Fu, Y.; An, N.; Yang, H.; Huo, X.; Yang, X.; Yan, H. Facile synthesis of $CeO_2$/carbonate doped $Bi_2O_2CO_3$ Z-scheme heterojunction for improved visible-light photocatalytic performance: Photodegradation of tetracycline and photocatalytic mechanism. *J. Coll. Interf. Sci*. **2021**, *588*, 283–294, https://doi.org/10.1016/j.jcis.2020.12.073.